

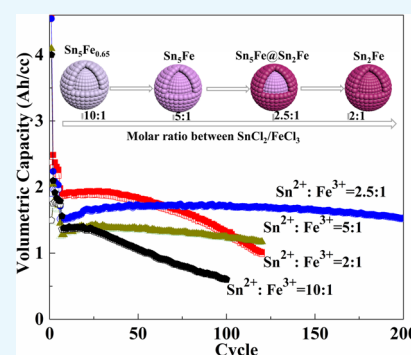
# Nanocrystal Conversion-Assisted Design of Sn–Fe Alloy with a Core–Shell Structure as High-Performance Anodes for Lithium-Ion Batteries

Fengxia Xin,<sup>†</sup> Hui Zhou,<sup>†</sup> Qiyue Yin,<sup>‡</sup> Yong Shi,<sup>†</sup> Fredrick Omenya,<sup>†</sup> Guangwen Zhou,<sup>‡</sup> and M. Stanley Whittingham<sup>\*,†</sup>

<sup>†</sup>Chemistry and Materials and <sup>‡</sup>Department of Mechanical Engineering & Materials Science and Engineering Program, State University of New York at Binghamton, Binghamton, New York 13902-6000, United States

## Supporting Information

**ABSTRACT:** Sn-based alloy materials are strong candidates to replace graphitic carbon as the anode for the next generation lithium-ion batteries because of their much higher gravimetric and volumetric capacity. A series of nanosize Sn<sub>3</sub>Fe alloys derived from the chemical transformation of preformed Sn nanoparticles as templates have been synthesized and characterized. An optimized Sn<sub>3</sub>Fe/Sn<sub>2</sub>Fe anode with a core–shell structure delivered 541 mAh·g<sup>-1</sup> after 200 cycles at the C/2 rate, retaining close to 100% of the initial capacity. Its volumetric capacity is double that of commercial graphitic carbon. It also has an excellent rate performance, delivering 94.8, 84.3, 72.1, and 58.2% of the 0.1 C capacity (679.8 mAh/g) at 0.2, 0.5, 1 and 2 C, respectively. The capacity is recovered upon lowering the rate. The exceptional cycling/rate capability and higher gravimetric/volumetric capacity make the Sn<sub>3</sub>Fe alloy a potential candidate as the anode in lithium-ion batteries. The understanding of Sn<sub>3</sub>Fe alloys from this work also provides insight for designing other Sn–M (M = Co, Ni, Cu, Mn, etc.) system.



## 1. INTRODUCTION

Rechargeable lithium-ion batteries have become the most important energy storage device for a wide range of technological applications, including portable communication electronics, hybrid electric vehicles (HEVs) or electric vehicles (EVs), and large-scale renewable grid storage because of their high energy density and long cycle life.<sup>1–8</sup> Because the Sony company successfully commercialized the Li-ion battery in 1990s, graphitic carbons have remained as the anode. However, the ever-increasing energy density needs for mass deployment of EVs have highlighted the limitations of carbon-based materials: their low gravimetric/volumetric capacity (340 mAh/g or 740 Ah/L) and poor high rate capability, which limits charging rates because of the potential nucleation and growth of lithium dendrites.<sup>9</sup> To satisfy the energy requirement of EVs, electrochemically active materials such as Si,<sup>10</sup> Ge,<sup>11</sup> and Sn<sup>12–14</sup> have received much attention for their higher gravimetric/volumetric capacity (SiLi<sub>4.4</sub>: 2005 mAh/g or 2444 mAh/cc, GeLi<sub>4.4</sub>: 1143 mAh/g or 1848 mAh/cc, SnLi<sub>4.4</sub>: 789 mAh/g or 2038 mAh/cc) and safer thermodynamic potential. Tin-based materials are scientifically one of the most promising candidates as they possess good conductivity and are nontoxic. However, a volume expansion of 257% on the complete reaction with Sn causes cracking/pulverization of the particles, potentially losing the connection with a current collector, and then failure of the electrode, resulting in a rapid deterioration in the cycling.<sup>14–19</sup>

Substantial efforts have been made to overcome these problems, including the design and exploration of nanostructure materials,<sup>20,21</sup> which could effectively reduce the absolute volume expansion, shorten the transport length of ions and electrons, and enhance permeation of electrolyte, thus improving the reaction kinetics during the lithiation/delithiation process. Forming Sn–M (M: inactive metal) alloy and Sn–C composite has two fascinating methods. Dispersing nano-Sn particles in a carbon matrix with some void space that can act as a “buffer zone” to alleviate the volume change is one approach to improve the electrochemically cycling and rate performance. For example, the electrodes of porous TiO<sub>2-x</sub>-C-Sn nanofibers,<sup>22</sup> Sn nanoparticles encapsulated in graphene-backed carbonaceous foam (F-G/Sn@C),<sup>23</sup> hierarchical Sn/C composite,<sup>24</sup> ultrasmall Sn nanoparticles embedded in spherical hollow carbon,<sup>25</sup> double network hydrogel-derived ultrafine Sn–Fe alloy in a three-dimensional carbon framework,<sup>26</sup> and so forth improve the cycling stability and capacity. Nevertheless, the introduction of a mass carbon source (graphene, amorphous porous carbon, ordered mesoporous carbon, and carbon nanotubes/nanofibers) and a void space will reduce the cell overall energy density, especially volumetric energy density. Moreover,

Received: December 27, 2018

Accepted: February 21, 2019

Published: March 5, 2019

multiple complicated steps in the synthesis process will impede their practical application. Sn–M (M = Fe,<sup>27,28</sup> Co,<sup>29,30</sup> Ni,<sup>31</sup> Cu,<sup>32</sup> Mn,<sup>33</sup> and so forth) alloy anode materials have been explored due to their good electronic conductivity, high tap density, and gravimetric/volumetric capacity (shown in Figure 1 and Table S1, Supporting Information). The volumetric

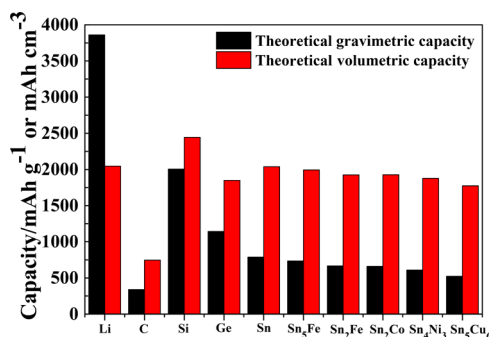


**Figure 1.** Theoretical gravimetric and volumetric capacities (the data was based on the amounts and the densities of the lithiated products). Black and red bars denote gravimetric and volumetric capacities, respectively.

capacity of Sn<sub>3</sub>Fe and Sn<sub>2</sub>Fe intermetallics is more than 2.5 times that of graphite based on the lithiated products. Fe is also nontoxic and low cost, which could help to prevent the Sn particles from aggregating and stabilizing the structure of the electrode, thus improving the electrochemical cycle life. Dahn reported earlier on the Sn–Fe system including Sn<sub>2</sub>Fe–C,<sup>34</sup> Sn<sub>y</sub>Fe (Sn<sub>2</sub>Fe, SnFe, Sn<sub>2</sub>Fe<sub>3</sub>, and Sn<sub>3</sub>Fe<sub>5</sub>),<sup>35</sup> and Sn<sub>2</sub>Fe:SnFe<sub>3</sub>C active/inactive composites.<sup>36</sup> However, the capacity faded rapidly with only 200 mAh·g<sup>-1</sup> after 80 cycles, and they concluded that Sn–Co was the ideal couple.<sup>37</sup> Our group previously reported, using high-energy ball milling, nanosized Sn–Fe–C nanoparticles could obtain 440 mAh/g after 170 cycles at a C/10 rate by adjusting the grinding media, reducing agent, total grinding time, graphite content, different carbon type, and Ti content.<sup>38,39</sup> Compared with mechanochemistry, nanocrystal conversion chemistry could result in lower reaction temperatures and better control of the morphology as well as avoiding melting of Sn metal.<sup>40–42</sup>

Therefore, in this work, we used a nanocrystal conversion chemistry approach and successfully synthesized a series of Sn<sub>y</sub>Fe alloys. The morphology, crystal structure, and composition of Sn<sub>y</sub>Fe intermetallic products were found to be greatly influenced by a temperature and reagent molar ratio. Furthermore, Sn<sub>3</sub>Fe–Sn<sub>2</sub>Fe electrodes with a core–shell structure showed excellent cycling and rate capacity. They delivered 541 mAh·g<sup>-1</sup> after 200 cycles at 0.5 C rate, corresponding to nearly 100% initial capacity, with a volumetric capacity almost twice that of carbon. This work on Sn<sub>y</sub>Fe alloys also provides insight for designing other Sn–M (M = Co, Ni, Cu, Mn, and so forth) system for next generation Li-ion batteries.

## 2. RESULTS AND DISCUSSION

**2.1. Materials Synthesis and Characterizations.** Figure 2a schematically displays the preparation steps of the Sn<sub>y</sub>Fe alloy. Generally, the growth process includes two stages: the formation of Sn nanoparticles and their subsequent transformation. The addition of the reducing agent (NaBH<sub>4</sub>) to the

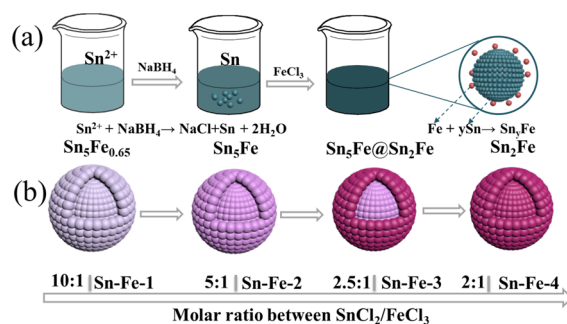
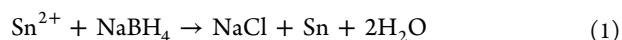


**Figure 2.** (a) Schematic illustration of the procedure for the preparation of Sn<sub>y</sub>Fe alloy nanoparticles. (b) Structure change of the Sn<sub>y</sub>Fe alloys in different reagent molar ratio between the SnCl<sub>2</sub> and FeCl<sub>3</sub>.

Sn salt quickly creates Sn nanospheres through a self-assembly process in the presence of poly(vinylpyrrolidone) (PVP) and



poly(2-ethyl-2-oxazoline) (PEtOx) surfactants, as shown in reaction 1.<sup>43</sup> Here, the high-boiling (310 °C) polyalcohol solvent, tetraethylene glycol (TEG), plays a significant role in the formation of the resulting materials.<sup>44</sup> After the first step, the Fe source was injected into the solution; then, intermetallic Sn<sub>y</sub>Fe nanoparticles were formed typically via a diffusion-based process where Fe diffuses into Sn.<sup>41</sup>



By adjusting the molar ratio of FeCl<sub>3</sub> to SnCl<sub>2</sub>, we could obtain Sn<sub>y</sub>Fe intermetallics with different structures and compositions, including core–shell structures (Figure 2b). The four materials synthesized with molar ratios of 10:1, 5:1, 2.5:1, and 2:1 are designated as Sn-Fe-1, Sn-Fe-2, Sn-Fe-3 (FeSn<sub>5</sub>@FeSn<sub>2</sub>), and Sn-Fe-4.

The Rietveld analysis of powder X-ray diffraction (XRD, Figure 3) of these four Sn<sub>y</sub>Fe materials formed at 110 °C

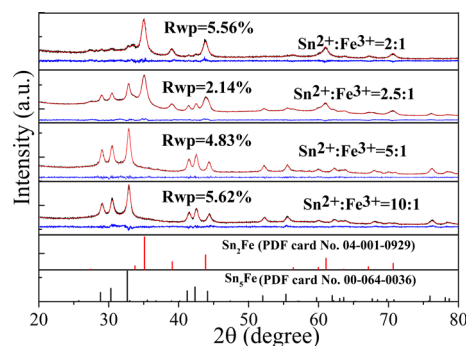


**Figure 3.** XRD patterns and refinements of the materials synthesized at 110 °C for reagent molar ratios of SnCl<sub>2</sub> to FeCl<sub>3</sub> from 10:1 to 2:1. Black line: observed profile; red line: calculated profile; blue line: difference profile.

showed that the diffraction peaks were those of Sn<sub>3</sub>Fe (PDF Card No. 00-064-0036) and Sn<sub>2</sub>Fe (PDF Card No. 04-001-0929) with the *P4/mcc* space group. The weighted *R*-factor *R*<sub>wp</sub> of the four samples are 5.62, 4.83, 2.14, and 5.56%. The diffraction peaks at 29.1, 30.5, 32.9, 41.6, 42.6, 44.5, 52.4, and 55.6° can be assigned to the (210), (002), (211), (310), (212), (311), (312), and (213) planes of the Sn<sub>3</sub>Fe phase,

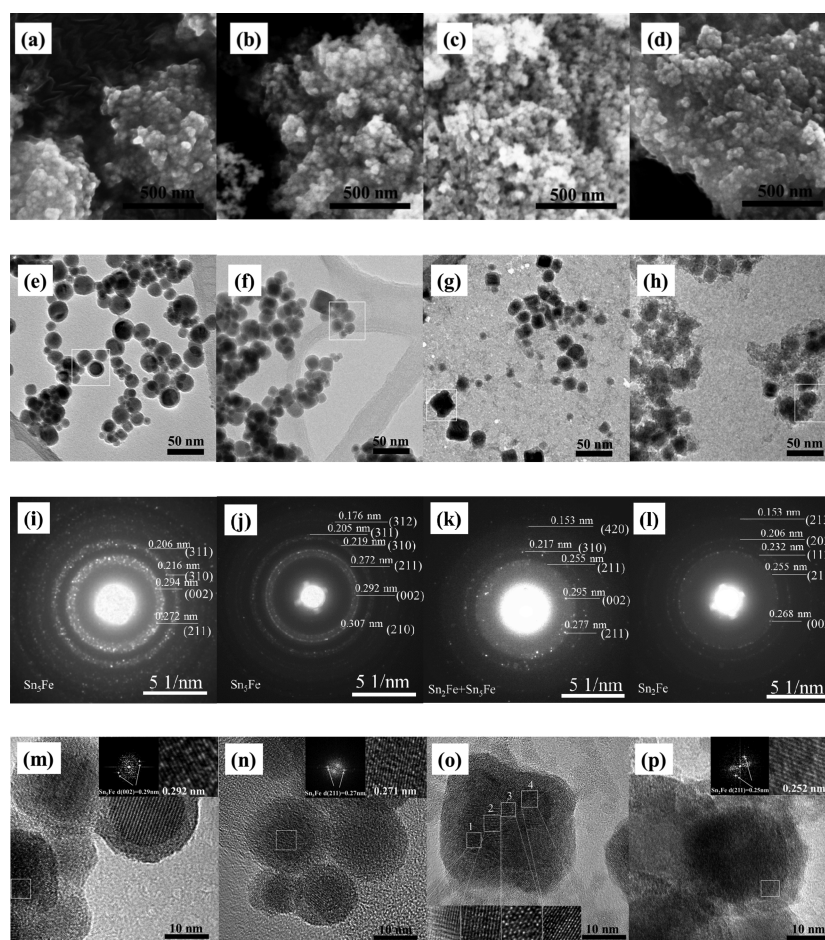


**Figure 4.** (a–d) SEM images, (e–h) TEM images, (i–l) SAED images, and (m–p) HRTEM images zooming in local area in corresponding TEM images of the four materials: Sn-Fe-1, Sn-Fe-2, Sn-Fe-3, and Sn-Fe-4.

respectively, and 33.7, 35.1, 39.2, 43.9, 61.1, and 70.7° are associated with the (002), (211), (112), (202), (213), and (004) planes of the  $\text{Sn}_2\text{Fe}$  phase, respectively. The refined lattice parameters of the  $\text{Sn}_5\text{Fe}$  and  $\text{Sn}_2\text{Fe}$  phases in the four samples are shown in Table S2. There was no evidence of any intermediate phase between  $\text{Sn}_5\text{Fe}$  and  $\text{Sn}_2\text{Fe}$ .

For molar ratios ( $\text{SnCl}_2:\text{FeCl}_3$ ) of 10:1 and 5:1, only the tetragonal  $\text{Sn}_5\text{Fe}$  phase was observed. The Sn-Fe-1 sample had a Sn/Fe molar ratio of 7.7, which is  $\text{Sn}_5\text{Fe}_{0.65}$ , not the stoichiometric  $\text{Sn}_5\text{Fe}$ . This Fe defect structure is supported by energy dispersive X-ray spectroscopy (EDS) measurement (Supporting Information, Table S3). The Rietveld refinement also showed that the weight ratio of  $\text{Sn}_5\text{Fe}$  nanoparticles decreased from 40.3 to 13.6% as the reagent ( $\text{SnCl}_2:\text{FeCl}_3$ ) molar ratio decreased from 2.5:1 to 2:1. Thus, the  $\text{Sn}_5\text{Fe}$  phase is found at all reactant molar ratios at 110 °C, but the  $\text{Sn}_2\text{Fe}$  phase is not found at the highest Sn ratios. In contrast, at 170 °C, even at the highest Sn ratio, the  $\text{Sn}_2\text{Fe}$  peak at 34.9° could be observed (Figure S1), and pure phase  $\text{Sn}_2\text{Fe}$  was formed at the lower Sn ratios. This suggests that the stability of the  $\text{Sn}_5\text{Fe}$  alloy decreases with increasing temperature and that the phases formed can be controlled by both temperature and reactant ratio. This change of crystal structure and composition for the  $\text{Sn}_n\text{Fe}$  alloy system might provide insight also into the  $\text{Sn}_n\text{M}$  ( $M = \text{Fe}, \text{Co}$  or  $\text{FeCo}$  and so on) alloys and their formation.

The morphology and composition of the  $\text{Sn}_n\text{Fe}$  materials were further characterized using scanning electron microscopy

(SEM) and transmission electron microscopy (TEM). As shown in Figure 4a–h, the primary particle sizes of the four materials are tens of nanometers, and the morphology changes with increasing Fe reactant content from spherical to cubic to ultrasmall/irregular particles. This may be due to the anisotropic Kirkendall effect.<sup>45</sup> The selected area electron diffraction (SAED) (Figure 4i–l) gives a good agreement with the XRD results:  $\text{Sn}_5\text{Fe}$  for Sn-Fe-1 and Sn-Fe-2,  $\text{Sn}_5\text{Fe}@ \text{Sn}_2\text{Fe}$  for Sn-Fe-3, and  $\text{Sn}_2\text{Fe}$  for Sn-Fe-4. High-resolution TEM (HR-TEM) images (Figure 4m–p) show that all the particles have a crystalline core covered by an amorphous oxide shell formed during exposure to air.<sup>46</sup> In addition, clear lattice fringes with interplanar distances of  $\approx 0.292$ ,  $\approx 0.271$ , and  $\approx 0.252$  nm in Figure 4m,n,p can be indexed to the (002) plane of crystalline  $\text{Sn}_5\text{Fe}$ , the (211) plane of crystalline  $\text{Sn}_5\text{Fe}$ , and the (211) plane of crystalline  $\text{Sn}_2\text{Fe}$ , respectively, which further verify the compositions of these samples.

To determine the composite distribution of Sn-Fe-3, the  $\text{Sn}_5\text{Fe}@ \text{Sn}_2\text{Fe}$  material, fast Fourier transform (FFT) diffractions are shown in Figure 5 on regions 1, 2, 3, and 4 in Figure 4o. The corresponding FFT spots show that regions 1, 2, 3, and 4 in the single particle are dominated by  $\text{Sn}_2\text{Fe}$ ,  $\text{Sn}_5\text{Fe}$ ,  $\text{Sn}_5\text{Fe}$ , and  $\text{Sn}_2\text{Fe}$  phase, respectively, which indicates a core–shell structure for the  $\text{Sn}_5\text{Fe}@ \text{Sn}_2\text{Fe}$  material, where the core is  $\text{Sn}_5\text{Fe}$  with a shell of  $\text{Sn}_2\text{Fe}$ . Considering the composition change from  $\text{Sn}_5\text{Fe}$  to  $\text{Sn}_5\text{Fe}@ \text{Sn}_2\text{Fe}$  to  $\text{Sn}_2\text{Fe}$  with increased Fe reactant content, the formation process may

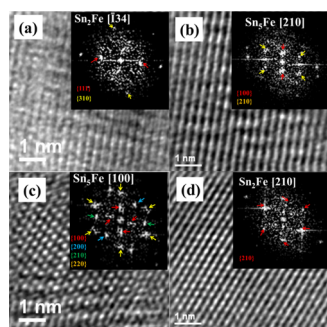


**Figure 5.** (a–d) HRTEM image of regions 1, 2, 3, and 4 in Figure 4o. Inset images are the corresponding FFT diffraction spots.

be that at a low Fe reactant content,  $\text{Sn}_3\text{Fe}$  is preferred to be formed, because  $\text{Sn}_3\text{Fe}$  is the phase intermediate between Sn and  $\text{Sn}_2\text{Fe}$ ; <sup>47</sup> when more Fe reactant is added,  $\text{Sn}_3\text{Fe}$  will transform to  $\text{Sn}_2\text{Fe}$  from the surface of the particle; when more and more Fe reactant is added, the transformation from  $\text{Sn}_3\text{Fe}$  to  $\text{Sn}_2\text{Fe}$  will go through the whole particle forming  $\text{Sn}_2\text{Fe}$ .

Figure 6a–d represents the scanning transmission electron microscopy (STEM) image of the four materials, and some particles were selected to do the EDX elemental line scanning of Fe and Sn for them. The molar ratios (shown in Figure 6e–h) of Fe and Sn were calculated based on the EDS line scanning experiment to determine the distribution. The calculated molar ratios (Figure 6e–h) of Sn/Fe for Sn-Fe-1, Sn-Fe-2, and Sn-Fe-4 are approximately 8, 5.0, and 2.3, indicating the existence of massive Fe defects for Sn-Fe-1, which are the perfect  $\text{Sn}_3\text{Fe}$  and  $\text{Sn}_2\text{Fe}$  phase for Sn-Fe-2 and Sn-Fe-4 samples. The most interesting one is the Sn-Fe-3 sample, which gives a higher molar ratio of Sn/Fe in the core of a particle and it verifies our speculation of a core ( $\text{Sn}_3\text{Fe}$ )–shell ( $\text{Sn}_2\text{Fe}$ ) structure.

**2.2. Electrochemical Performance of the  $\text{Sn}_y\text{Fe}$  Nanoparticles.** Electrochemical reactions for the first five cycles for the four  $\text{Sn}_y\text{Fe}$  materials synthesized in 110 °C were investigated by cyclic voltammetry (CV, Figure S2) at a scan rate of 0.05 mV/s in a voltage window of 0.005–1.5 V versus

$\text{Li}^+/\text{Li}$ . The broad cathodic peak located around 1.25 V in the first cycle is ascribed to the formation of solid-electrolyte interface (SEI) films, which disappeared for the following cycles, consuming Li ions and resulting in mainly irreversible capacity loss. The reduction peaks below 0.3 V for the lithium insertion process are assigned to the formation of  $\text{Li}_x\text{Sn}$  alloys. Two anodic peaks at 0.55 and 0.65 V were attributed to Li extraction reaction, which corresponds to the reversible dealloying process. Figure 7 displays the voltage profiles of the  $\text{Sn}_y\text{Fe}$  anodes in the initial five charge/discharge cycles between 0.01 and 1.5 V at a current rate of 0.1 C (1 C = 600  $\text{mAh}\cdot\text{g}^{-1}$ ). The theoretical capacities of Sn-Fe-1, Sn-Fe-2, Sn-Fe-3, and Sn-Fe-4 materials are 935.9, 900.3, 851.8, and 827.1  $\text{mAh}\cdot\text{g}^{-1}$  based on the EDS composition and formation of  $\text{Li}_{4.4}\text{Sn} + \text{Fe}$ . The first lithium insertion/removal cycle of Sn-Fe-1, Sn-Fe-2, Sn-Fe-3, and Sn-Fe-4 delivered capacities of 1498/561, 1499.4/537.9, 1617.9/645.8, and 1592.2/830.3  $\text{mAh}\cdot\text{g}^{-1}$ , respectively, corresponding to the Coulombic efficiencies (CE) of 37.4, 35.9, 39.9, and 52.1%. The large irreversible capacity loss in the first cycle is mainly attributed to electrolyte decomposition/formation of the SEI film at the electrode/electrolyte surface and reduction of the surface oxidized layer. <sup>46,48–50</sup> However, the results are comparable with nanostructure materials as anodes for lithium-ion batteries. <sup>46,51,52</sup>

The initial Coulombic efficiency decreases with an increasing Sn content, suggesting that irreversible reactions on tin cause this excess capacity on the first reaction with lithium. This is consistent with the slow drop in voltage in the first discharge process, when the SEI is formed above 1 V. The plateau around 0.3 V represents the alloying reaction between Li and Sn–Fe intermetallic forming  $\text{Li}_x\text{Sn}$ . As shown in the figure, except the first cycle, the voltage plateaus due to SEI formation above 1.0 V are absent, and the cell voltage quickly falls to 0.6 V. The charging curves display two main plateaus at ~0.55 and ~0.7 V, which are ascribed to the delithiation reactions and are consistent with the CV results.

Figure 8a,b shows the gravimetric and volumetric capacities of the four anodes with different Sn–Fe compositions at a

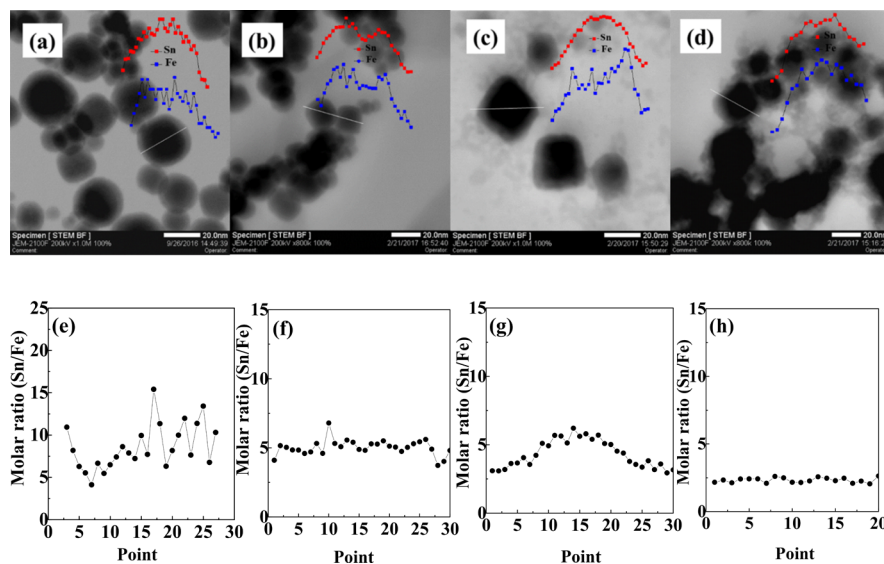


**Figure 6.** (a–d) STEM images of the Sn-Fe-1, Sn-Fe-2, Sn-Fe-3, and Sn-Fe-4 materials with the EDS line scanning results, showing the intensity of Sn L and Fe K signal. (e–h) The molar ratios calculated from the corresponding EDS line scanning in (a–d).

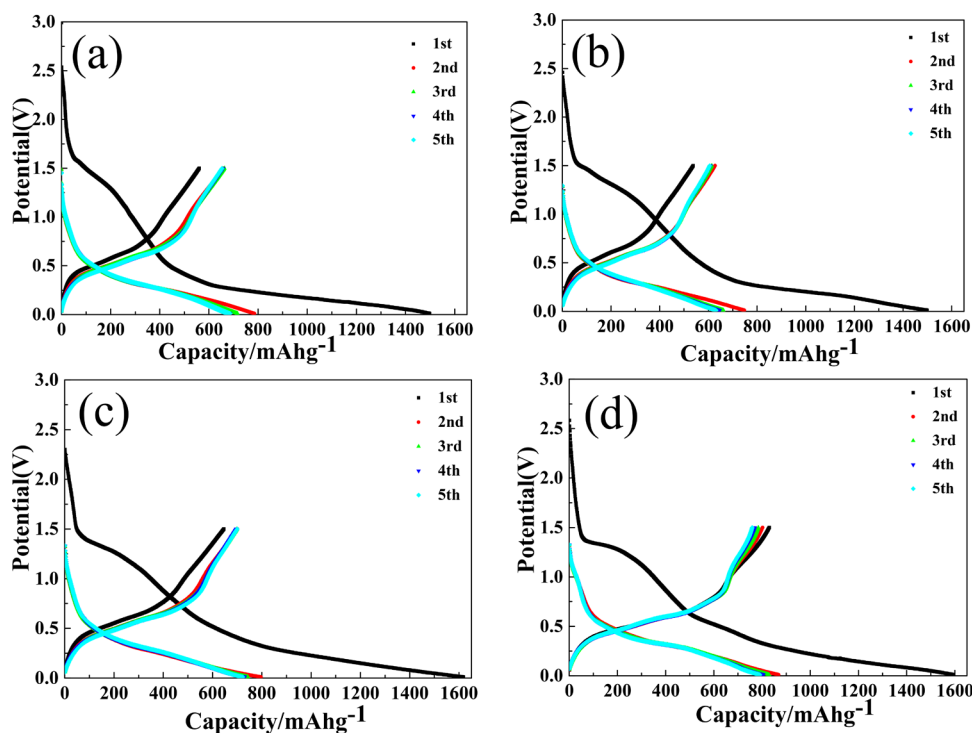


**Figure 7.** Galvanostatic charge–discharge curves of the first five cycles at  $C/10$  ( $1\text{ C} = 600\text{ mA}\cdot\text{g}^{-1}$ ) for (a) Sn-Fe-1, (b) Sn-Fe-2, (c) Sn-Fe-3, and (d) Sn-Fe-4 materials.

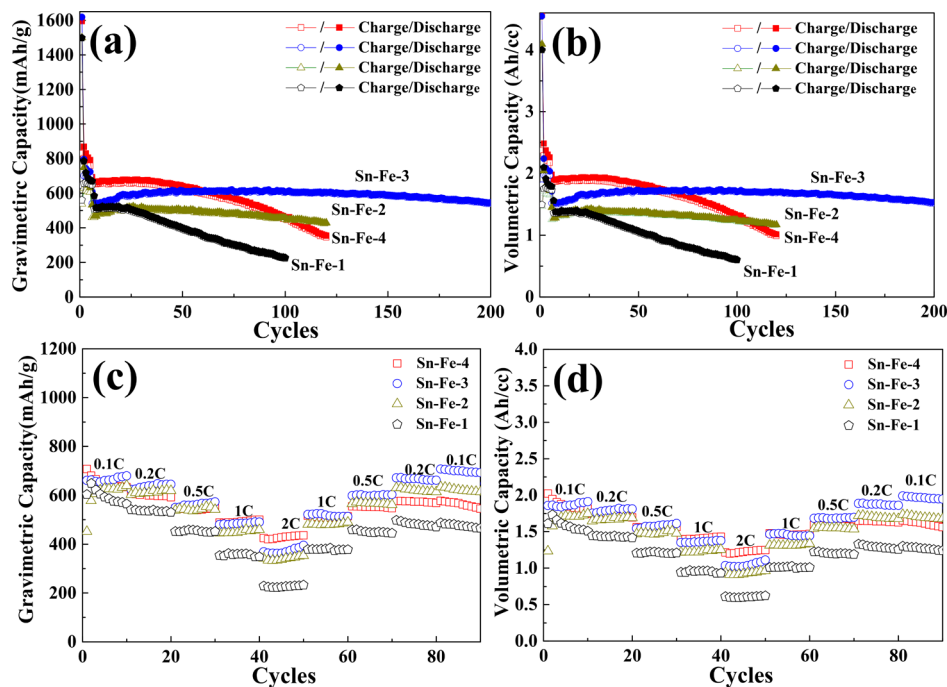


**Figure 8.** Cycling performance of the samples at the  $C/2$  rate is shown by (a) gravimetric and (b) calculated volumetric capacity. Rate performance of the samples is shown by (c) gravimetric capacity and (d) calculated volumetric capacity.

current density of  $0.5\text{ C}$  in a voltage range of  $0.01$  to  $1.5\text{ V}$  (the first five cycles were at  $0.1\text{ C}$  rate to activate the materials). The Sn-Fe-1 anode with the Fe defects delivered a capacity of  $\sim 500\text{ mAh}\cdot\text{g}^{-1}$  for 25 cycles, but the capacity quickly dropped to  $\sim 224\text{ mAh}\cdot\text{g}^{-1}$  after 100 cycles. Wang et al. also reported that the  $\text{Sn}_5\text{Fe}$  anode (defect structure  $\text{Fe}_{0.74}\text{Sn}_5$ ) with a particle size of  $41 \pm 8\text{ nm}$  could achieve  $750\text{ mAh}\cdot\text{g}^{-1}$  in  $0.05\text{ C}$  for 15 cycles but then decayed rapidly.<sup>40</sup> It appears that a

minimum amount of Fe is necessary to stabilize the overall structure and that there is insufficient in this Fe-deficient lattice. The Fe-richer Sn-Fe-2 material had a capacity of  $\sim 516\text{ mAh}\cdot\text{g}^{-1}$  for 25 cycles and still had  $457\text{ mAh}\cdot\text{g}^{-1}$  after 100 cycles. A superior material is the core–shell structure of Sn-Fe-3 sample, where the reversible capacity climbed to  $\sim 600\text{ mAh}\cdot\text{g}^{-1}$  by 40 cycles, having an even higher capacity that initially at the  $0.1\text{ C}$  lower current density. After 200 cycles, the capacity

was still 541 mAh·g<sup>-1</sup>, corresponding to nearly 100% of the initial capacity (the sixth cycle, for the first five cycles at 0.1 C) and ~90.2% of the highest charging capacity. The average capacity loss was only 0.049% per cycle according to 90.2% retention ratio, and cycling efficiency exceeded 99.5% for most of the cycles. Although it had the highest initial capacity, the Sn-Fe-4 electrode, it gradually decayed. The practical tap density of these four Sn<sub>y</sub>Fe nanostructure materials is between 1.6 and 1.7 g/cc, which was much higher than that of graphite 0.8 g/cc. Therefore, the calculated volumetric capacity of the core-shell anode, Sn-Fe-3, is close to twice that of carbon (0.8 Ah/cc) after 200 cycles.

The rate capability of these Sn<sub>y</sub>Fe anodes was determined from 0.1 to 2 C and back to 0.1 C, and the results are shown in Figure 8c,d. The corresponding charge and discharge curves in different current rate are presented in Figure S3. Among the four samples, the core-shell shows the best maintenance of capacity after 90 cycles, and the highest rate capability except at the 2C rate when the Sn-Fe-4 material was superior, but it did not retain well the capacity when returned to low rates. The highest tin content materials performed the worst on the rate test and did not get back their full capacity when the rate was lowered. This is expected from the capacity decay observed in Figure 8a. All four materials were removed for characterization after the tests of Figure 8 and after Li removal to 1.5 V. Much of the crystallinity had been lost, and Sn metal was observed in the Sn-Fe-1 and Sn-Fe-4 materials (see Figure S4); this suggests that the superior performance of the intermediate composition is due to the lack of the presence of tin metal.

### 3. CONCLUSIONS

The high gravimetric, 541 mAh/g after 200 cycles, and volumetric capacity, superior rate capability, and reversibility of the Sn<sub>y</sub>Fe materials reported here suggest that an electrochemically inactive element such as Fe is critical in maintaining the capacity of the material. In addition, the capacity and capacity retention can be increased by using a core-shell structure in which the more reactive, in this case, the Sn<sub>5</sub>Fe, component is protected by the lower less reactive Sn content material.

### 4. EXPERIMENTAL SECTION

Tin (II) chloride (SnCl<sub>2</sub>, anhydrous, 99%), iron (III) chloride (FeCl<sub>3</sub>, anhydrous, 97%), poly(vinylpyrrolidone) (PVP, MW=360 000), poly(2-ethyl-2-oxazoline) (PEtOx, MW = 50 000), tetraethylene glycol (TEG, 99%), and sodium borohydride (NaBH<sub>4</sub>, 98%) were used as reaction chemicals. The Sn<sub>y</sub>Fe alloy nanoparticles were synthesized according to the Chou et al. procedure.<sup>41</sup> It was carried out under an argon atmosphere via a Schlenk line. Typically, 2.1285 g of PVP and 0.9135 g of PEtOx were added into 50 mL of TEG in a three-neck flask with vigorously stirring in 110 °C. After PVP and PEtOx were dissolved, a SnCl<sub>2</sub> solution (0.6 g of SnCl<sub>2</sub> in 6 mL of TEG) was injected and hold for 15 min. The freshly prepared NaBH<sub>4</sub> solution (0.5 g of NaBH<sub>4</sub> in 25 mL of TEG) as a reducing agent was introduced drop by drop. The color of the solution suddenly changed to black. It was stirred at 110 °C for 25 min before the injection of FeCl<sub>3</sub> solution (0.055 g of FeCl<sub>3</sub> in 6 mL of TEG). After 45 min, the suspension was cooled down to room temperature. Changing FeCl<sub>3</sub> solution (0.11 g of FeCl<sub>3</sub> in 6 mL of TEG, 0.22 g of FeCl<sub>3</sub> in 6 mL of

TEG, 0.275 g of FeCl<sub>3</sub> in 6 mL of TEG), we obtained a series of samples with a molar ratio between SnCl<sub>2</sub> and FeCl<sub>3</sub> from 10:1, 5:1, 2.5:1, to 2:1. Sn<sub>y</sub>Fe alloys in 170 °C were also prepared under the same reagent molar ratio. All the samples were washed four to five times using ethanol under sonication and harvested by centrifugation with a speed of 12000 rad/min; no residual B, C, or N was detected by EDS.

The structure of the samples was characterized by X-ray diffraction with a BRUKER diffractometer (D8 Advance) equipped with Cu K<sub>α</sub> source ( $\lambda = 1.54178 \text{ \AA}$ ), and data were collected over a  $2\theta$  range of 10–90° with a step size of 0.02° and a dwell time of 1 s. The Rietveld refinement of collected XRD data was performed using software TOPAS-Academic V4.2. A Zeiss Supra 55 VP field-emission scanning electron microscopy (SEM) operating voltage of 5 kV and transmission electron microscopy (TEM, JEOL JEM2100F) with an energy dispersive X-ray spectroscopy (EDS) detector were applied to detect the morphology of the samples. A structure of Fe-Sn alloy nanoparticles was studied by selected area electron diffraction (SAED) on a JEM2100F operated at 200 kV. EDX elemental line scanning of Fe and Sn element was operated in an STEM mode. The molar ratio of Sn to Fe ( $n_{\text{Sn}}/n_{\text{Fe}}$ ) can be calculated as follows:  $n_{\text{Sn}}/n_{\text{Fe}} = (I_{\text{Sn}} \times k_{\text{Sn}} \times M_{\text{Fe}}) / (I_{\text{Fe}} \times k_{\text{Fe}} \times M_{\text{Sn}})$ , in which  $I_{\text{Sn}}$  and  $I_{\text{Fe}}$  are the counts of the EDS signal collected during an STEM line scan,  $k_{\text{Sn}}$  and  $k_{\text{Fe}}$  are the  $k$  factor, and  $M_{\text{Sn}}$  and  $M_{\text{Fe}}$  are the atomic molar weights of the elements Sn and Fe. For the TEM sample preparation process, the Sn<sub>y</sub>Fe powder was well dispersed in ethanol solvent with vigorous sonication and then dropped it to a lacey carbon TEM grid, which was dried and placed onto a Gavan holder. The tap density was measured by a TD1 tap density tester.

The Sn<sub>y</sub>Fe nanoparticles were mixed with carbon black and sodium carboxymethyl cellulose (CMC, MW ~ 100,000) to form a slurry in a weight ratio of 80:10:10 with an appropriate amount of distilled water solvent. The working electrode was prepared by casting the slurry on a copper current collector using a doctor blade and drying in a vacuum oven at 80 °C for 12 h. Then, it was punched into an area of 1.2 cm<sup>2</sup> with a loading weight of 1.2 mg·cm<sup>-2</sup>. The 2325-type coin cells were assembled in a Helium-filled glove box under ambient temperature with the Celgard 2400 membrane as the separator and Li foil as a counter and a reference electrode. LiPF<sub>6</sub> (1.0 M) dissolved in ethylene carbonate/diethyl carbonate (EC/DEC, 1:1 in volume) with 10% fluoroethylene carbonate (FEC) as an additive was used as the electrolyte solution to improve cycling stability. All galvanostatic charging/discharging tests were obtained on a multichannel Biologic system with a voltage range of 0.01–1.5 V at different current rate (1 C = 600 mA·g<sup>-1</sup>) and cyclic voltammetry (CV) between 0.005 and 1.5 V at a scan rate of 0.025 mV/s.

### ■ ASSOCIATED CONTENT

#### Supporting Information

The Supporting Information is available free of charge on the ACS Publications website at DOI: 10.1021/acsomega.8b03637.

Density, gravimetric and volumetric capacities for the anode materials in lithium ion batteries; the mass ratio between Sn<sub>2</sub>Fe and Sn<sub>5</sub>Fe from XRD refinements and the atom ratio from EDS; XRD patterns of phases formed at 170 °C; CV curves of the first five cycles with a scan rate of 0.05 mV·s<sup>-1</sup> in Sn-Fe-1, Sn-Fe-2, Sn-Fe-3,

and Sn-Fe-4; the charge and discharge curves in different current rate; and SEM images and XRD patterns of the electrode after rate performance test for the Sn-Fe-1, Sn-Fe-2, Sn-Fe-3, and Sn-Fe-4 materials (PDF)

## AUTHOR INFORMATION

### Corresponding Author

\*E-mail: stanwhit@gmail.com.

### ORCID

Yong Shi: 0000-0001-6422-8942

Guangwen Zhou: 0000-0002-9243-293X

M. Stanley Whittingham: 0000-0002-5039-9334

### Notes

The authors declare no competing financial interest.

## ACKNOWLEDGMENTS

This work is supported by the U.S. Department of Energy's Office of Energy Efficiency and Renewable Energy (EERE) program under awards no. DE-EE0006852 and DE-EE0007765. We also thank Drs. Dongsheng Ji, Jia Ding, Xiaoya Wang, and Natasha Chernova for many helpful discussions.

## REFERENCES

- (1) Suo, L.; Borodin, O.; Gao, T.; Olguin, M.; Ho, J.; Fan, X.; Luo, C.; Wang, C.; Xu, K. "Water-in-salt" electrolyte enables high-voltage aqueous lithium-ion chemistries. *Science* **2015**, *350*, 938–943.
- (2) Lukatskaya, M. R.; Dunn, B.; Gogotsi, Y. Multidimensional materials and device architectures for future hybrid energy storage. *Nat. Commun.* **2016**, *7*, 12647.
- (3) Armand, M.; Tarascon, J.-M. Building Better Batteries. *Nature* **2008**, *451*, 652–657.
- (4) Wang, X.; Hao, H.; Liu, J.; Huang, T.; Yu, A. A novel method for preparation of macroporous lithium nickel manganese oxygen as cathode material for lithium ion batteries. *Electrochim. Acta* **2011**, *56*, 4065–4069.
- (5) Eom, K.; Lee, J. T.; Oschatz, M.; Wu, F.; Kaskel, S.; Yushin, G.; Fuller, T. F. A stable lithiated silicon-chalcogen battery via synergetic chemical coupling between silicon and selenium. *Nat. Commun.* **2017**, *8*, 13888.
- (6) Lee, S. J.; Kim, H. J.; Hwang, T. H.; Choi, S.; Park, S. H.; Deniz, E.; Jung, D. S.; Choi, J. W. Delicate Structural Control of Si-SiO<sub>x</sub>-C Composite via High-Speed Spray Pyrolysis for Li-Ion Battery Anodes. *Nano Lett.* **2017**, *17*, 1870–1876.
- (7) Devaux, D.; Wang, X.; Thelen, J. L.; Parkinson, D. Y.; Cabana, J.; Wang, F.; Balsara, N. P. Lithium Metal-Copper Vanadium Oxide Battery with a Block Copolymer Electrolyte. *J. Electrochem. Soc.* **2016**, *163*, A2447–A2455.
- (8) Zhou, L.; Zhang, K.; Hu, Z.; Tao, Z.; Mai, L.; Kang, Y. M.; Chou, S. L.; Chen, J. Recent Developments on and Prospects for Electrode Materials with Hierarchical Structures for Lithium-Ion Batteries. *Adv. Energy Mater.* **2018**, *8*, 1701415.
- (9) Whittingham, M. S. History, Evolution, and Future Status of Energy Storage. *Proc. IEEE* **2012**, *100*, 1518–1534.
- (10) Tian, H.; Tan, X.; Xin, F.; Wang, C.; Han, W. Micro-sized nano-porous Si/C anodes for lithium ion batteries. *Nano Energy* **2015**, *11*, 490–499.
- (11) Kennedy, T.; Brandon, M.; Ryan, K. M. Advances in the Application of Silicon and Germanium Nanowires for High-Performance Lithium-Ion Batteries. *Adv. Mater.* **2016**, *28*, 5696–5704.
- (12) Fan, Q.; Chupas, P. J.; Whittingham, M. S. Characterization of Amorphous and Crystalline Tin–Cobalt Anodes. *Electrochim. Solid-State Lett.* **2007**, *10*, A274–A278.
- (13) Ying, H.; Zhang, S.; Meng, Z.; Sun, Z.; Han, W.-Q. Ultrasmall Sn nanodots embedded inside N-doped carbon microcages as high-performance lithium and sodium ion battery anodes. *J. Mater. Chem. A* **2017**, *5*, 8334–8342.
- (14) Ying, H.; Han, W.-Q. Metallic Sn-Based Anode Materials: Application in High-Performance Lithium-Ion and Sodium-Ion Batteries. *Adv. Sci.* **2017**, *4*, 1700298.
- (15) Yang, S.; Zavalij, P. Y.; Whittingham, M. S. Anodes for lithium batteries: tin revisited. *Electrochim. Commun.* **2003**, *5*, 587–590.
- (16) Xin, F.-X.; Tian, H.-J.; Wang, X.-L.; Xu, W.; Zheng, W.-G.; Han, W.-Q. Enhanced Electrochemical Performance of Fe<sub>0.74</sub>Sn<sub>5</sub>@Reduced Graphene Oxide Nanocomposite Anodes for Both Li-Ion and Na-Ion Batteries. *ACS Appl. Mater. Interfaces* **2015**, *7*, 7912–7919.
- (17) Wu, X.; Zhang, S.; Qi, T.; Fang, H.; Liu, G.; Xing, Y. Novel insight toward engineering of arrayed Cu@Sn nanoelectrodes: Rational microstructure refinement and its remarkable "harvesting effect" on lithium storage capability. *J. Power Sources* **2016**, *307*, 753–761.
- (18) Park, C.-M.; Kim, J.-H.; Kim, H.; Sohn, H.-J. Li-Alloy Based Anode Materials for Li Secondary Batteries. *Chem. Soc. Rev.* **2010**, *39*, 3115–3141.
- (19) Zhou, X.; Yu, L.; Yu, X.-Y.; Lou, X. W. D. Encapsulating Sn Nanoparticles in Amorphous Carbon Nanotubes for Enhanced Lithium Storage Properties. *Adv. Energy Mater.* **2016**, *6*, 1601177.
- (20) Shi, H.; Zhang, A.; Zhang, X.; Yin, H.; Wang, S.; Tang, Y.; Zhou, Y.; Wu, P. Pyrolysis of cyano-bridged hetero-metallic aerogels: a general route to immobilize Sn-M (M = Fe, Ni) alloys within a carbon matrix for stable and fast lithium storage. *Nanoscale* **2018**, *10*, 4962–4968.
- (21) Wang, Z.; Wang, Z.; Liu, W.; Xiao, W.; Lou, X. W. Amorphous CoSnO<sub>3</sub>@C nanoboxes with superior lithium storage capability. *Energy Environ. Sci.* **2013**, *6*, 87–91.
- (22) Li, X.; Chen, Y.; Wang, H.; Yao, H.; Huang, H.; Mai, Y.-W.; Hu, N.; Zhou, L. Inserting Sn Nanoparticles into the Pores of TiO<sub>2-x</sub>C Nanofibers by Lithiation. *Adv. Funct. Mater.* **2016**, *26*, 376–383.
- (23) Luo, B.; Qiu, T.; Ye, D.; Wang, L.; Zhi, L. Tin nanoparticles encapsulated in graphene backbone carbonaceous foams as high-performance anodes for lithium-ion and sodium-ion storage. *Nano Energy* **2016**, *22*, 232–240.
- (24) Huang, X.; Cui, S.; Chang, J.; Hallac, P. B.; Fell, C. R.; Luo, Y.; Metz, B.; Jiang, J.; Hurley, P. T.; Chen, J. A Hierarchical Tin/Carbon Composite as an Anode for Lithium-Ion Batteries with a Long Cycle Life. *Angew. Chem. Int. Ed.* **2015**, *54*, 1490–1493.
- (25) Zhang, N.; Wang, Y.; Jia, M.; Liu, Y.; Xu, J.; Jiao, L.; Cheng, F. Ultrasmall Sn nanoparticles embedded in spherical hollow carbon for enhanced lithium storage properties. *Chem. Commun.* **2018**, *54*, 1205–1208.
- (26) Shi, H.; Fang, Z.; Zhang, X.; Li, F.; Tang, Y.; Zhou, Y.; Wu, P.; Yu, G. Double-Network Nanostructured Hydrogel-Derived Ultrafine Sn–Fe Alloy in Three-Dimensional Carbon Framework for Enhanced Lithium Storage. *Nano Lett.* **2018**, *18*, 3193–3198.
- (27) Liu, C.-j.; Xue, F.-h.; Huang, H.; Yu, X.-h.; Xie, C.-j.; Shi, M.-s.; Cao, G.-z.; Jung, Y.-g.; Dong, X.-l. Preparation and Electrochemical properties of Fe-Sn (C) Nanocomposites as Anode for Lithium-ion Batteries. *Electrochim. Acta* **2014**, *129*, 93–99.
- (28) Vogt, L. O.; Villeveille, C. Elucidation of the reaction mechanisms of isostructural FeSn<sub>2</sub> and CoSn<sub>2</sub> negative electrodes for Na-ion batteries. *J. Mater. Chem. A* **2017**, *5*, 3865–3874.
- (29) Xin, F.; Wang, X.; Bai, J.; Wen, W.; Tian, H.; Wang, C.; Han, W. A lithiation/delithiation mechanism of monodispersed M<sub>2</sub>Sn<sub>5</sub> (M = Fe, Co and FeCo) nanospheres. *J. Mater. Chem. A* **2015**, *3*, 7170–7178.
- (30) Shi, X.; Song, H.; Li, A.; Chen, X.; Zhou, J.; Ma, Z. Sn–Co nanocomposites embedded in porous N-doped carbon microboxes as a stable anode material for lithium-ion batteries. *J. Mater. Chem. A* **2017**, *5*, 5873–5879.
- (31) Li, J.-T.; Swiatowska, J.; Maurice, V.; Seyeux, A.; Huang, L.; Sun, S.-G.; Marcus, P. XPS and ToF-SIMS Study of Electrode

Processes on Sn-Ni Alloy Anodes for Li-Ion Batteries. *J. Phys. Chem. C* **2011**, *115*, 7012–7018.

(32) Heidari, G.; Mousavi Khoie, S. M.; Abrishami, M. E.; Javanbakht, M. Electrodeposition of Cu-Sn alloys: theoretical and experimental approaches. *J. Mater. Sci. Mater. Electron.* **2015**, *26*, 1969–1976.

(33) Beaulieu, L. Y.; Dahn, J. R. The reaction of lithium with Sn-Mn-C intermetallics prepared by mechanical alloying. *J. Electrochem. Soc.* **2000**, *147*, 3237–3241.

(34) Mao, O.; Dunlap, R. A.; Dahn, J. R. Mechanically alloyed Sn-Fe(-C) powders as anode materials for Li-ion batteries - I. The Sn<sub>2</sub>Fe-C system. *J. Electrochem. Soc.* **1999**, *146*, 405–413.

(35) Mao, O. Mechanically Alloyed Sn-Fe(-C) Powders as Anode Materials for Li-Ion Batteries: II. The Sn-Fe System. *J. Electrochem. Soc.* **1999**, *146*, 414.

(36) Mao, O.; Dahn, J. R. Mechanically Alloyed Sn-Fe(-C) Powders as Anode Materials for Li-ion batteries - III. Sn<sub>2</sub>Fe : SnFe<sub>3</sub>C Active/Inactive Composites. *J. Electrochem. Soc.* **1999**, *146*, 423–427.

(37) Todd, A. D. W.; Mar, R. E.; Dahn, J. R. Tin-transition metal-carbon systems for lithium-ion battery negative electrodes. *J. Electrochem. Soc.* **2007**, *154*, A597–A604.

(38) Zhang, R.; Upreti, S.; Whittingham, M. S. Tin-Iron Based Nano-Materials as Anodes for Li-Ion Batteries. *J. Electrochem. Soc.* **2011**, *158*, A1498–A1504.

(39) Dong, Z.; Zhang, R.; Ji, D.; Chernova, N. A.; Karki, K.; Sallis, S.; Piper, L.; Whittingham, M. S. The Anode Challenge for Lithium-Ion Batteries: A Mechanochemically Synthesized Sn-Fe-C Composite Anode Surpasses Graphitic Carbon. *Adv. Sci.* **2016**, *3*, 1500229.

(40) Wang, X.-L.; Feyngenson, M.; Chen, H.; Lin, C.-H.; Ku, W.; Bai, J.; Aronson, M. C.; Tyson, T. A.; Han, W.-Q. Nanospheres of a New Intermetallic FeSn<sub>3</sub> Phase: Synthesis, Magnetic Properties and Anode Performance in Li-ion Batteries. *J. Am. Chem. Soc.* **2011**, *133*, 11213–11219.

(41) Chou, N. H.; Schaak, R. E. Shape-Controlled Conversion of Beta-Sn Nanocrystals into Intermetallic M-Sn (M = Fe, Co, Ni, Pd) Nanocrystals. *J. Am. Chem. Soc.* **2007**, *129*, 7339–7345.

(42) Chou, N. H.; Schaak, R. E. A library of single-crystal metal-tin nanorods: Using diffusion as a tool for controlling the morphology of intermetallic nanocrystals. *Chem. Mater.* **2008**, *20*, 2081–2085.

(43) Noh, M.; Kwon, Y.; Lee, H.; Cho, J.; Kim, Y.; Kim, M. G. Amorphous Carbon-Coated Tin Anode Material for Lithium Secondary Battery. *Chem. Mater.* **2005**, *17*, 1926–1929.

(44) Wang, X.-L.; Feyngenson, M.; Aronson, M. C.; Han, W.-Q. Sn/SnO<sub>x</sub> core-shell nanospheres: synthesis, anode performance in Li ion batteries, and superconductivity. *J. Phys. Chem. C* **2010**, *114*, 14697–14703.

(45) Vasquez, Y.; Henkes, A. E.; Chris Bauer, J.; Schaak, R. E. Nanocrystal Conversion Chemistry: A Unified and Materials-General Strategy for the Template-Based Synthesis of Nanocrystalline Solids. *J. Solid State Chem.* **2008**, *181*, 1509–1523.

(46) Kravchuk, K.; Protesescu, L.; Bodnarchuk, M. I.; Krumeich, F.; Yarema, M.; Walter, M.; Guntlin, C.; Kovalenko, M. V. Monodisperse and Inorganically Capped Sn and Sn/SnO<sub>2</sub> Nanocrystals for High-Performance Li-Ion Battery Anodes. *J. Am. Chem. Soc.* **2013**, *135*, 4199–4202.

(47) Sun, W.; Zhang, L.; Liu, J.; Wang, H.; Bu, Y. First-principles investigation of mechanical, thermodynamic and electronic properties of FeSn<sub>3</sub> and CoSn<sub>3</sub> phases. *Comput. Mater. Sci.* **2016**, *111*, 175–180.

(48) Xu, L.; Kim, C.; Shukla, A. K.; Dong, A.; Mattox, T. M.; Milliron, D. J.; Cabana, J. Monodisperse Sn Nanocrystals as a Platform for the Study of Mechanical Damage during Electrochemical Reactions with Li. *Nano Lett.* **2013**, *13*, 1800–1805.

(49) Li, Q.; Li, Z.; Zhang, Z.; Li, C.; Ma, J.; Wang, C.; Ge, X.; Dong, S.; Yin, L. Low-Temperature Solution-Based Phosphorization Reaction Route to Sn<sub>4</sub>P<sub>3</sub>/Reduced Graphene Oxide Nanohybrids as Anodes for Sodium Ion Batteries. *Adv. Energy Mater.* **2016**, *6*, 1600376.

(50) Protesescu, L.; Rossini, A. J.; Kriegner, D.; Valla, M.; De Kergommeaux, A.; Walter, M.; Kravchuk, K. V.; Nachtgeal, M.;

Stangl, J.; Malaman, B.; Reiss, P.; Lesage, A.; Emsley, L.; Cop éret, C.; Kovalenko, M. V. Unraveling the Core–Shell Structure of Ligand-Capped Sn/SnO<sub>x</sub> Nanoparticles by Surface-Enhanced Nuclear Magnetic Resonance, Mössbauer, and X-ray Absorption Spectroscopies. *ACS Nano* **2014**, *8*, 2639–2648.

(51) Wu, C.; Maier, J.; Yu, Y. Sn-Based Nanoparticles Encapsulated in a Porous 3D Graphene Network: Advanced Anodes for High-Rate and Long Life Li-Ion Batteries. *Adv. Funct. Mater.* **2015**, *25*, 3488–3496.

(52) Bodnarchuk, M. I.; Kravchuk, K. V.; Krumeich, F.; Wang, S.; Kovalenko, M. V. Colloidal Tin-Germanium Nanorods and Their Li-Ion Storage Properties. *ACS Nano* **2014**, *8*, 2360–2368.